Available online at www.sciencedirect.com
ScienceDirect
Icarus 192 (2007) 92–105
ICARUS
www.elsevier.com/locate/icarus

Unstable extension of Enceladus' lithosphere

Michael T. Bland [a,*], Ross A. Beyer [b,c], Adam P. Showman [a]

[a] *Department of Planetary Science, Lunar and Planetary Laboratory, University of Arizona, Tucson, AZ 85721, USA*
[b] *Carl Sagan Center at the SETI Institute, 515 N. Whisman Rd., Mountain View, CA 94035, USA*
[c] *NASA Ames Research Center, MS 245-3, Moffet Field, CA 94035, USA*

Received 7 February 2007; revised 6 June 2007

Available online 26 July 2007

Abstract

Regions near Enceladus' equator, Sarandib and Diyar Planitia, contain extensive sets of parallel ridges and troughs that may be diagnostic of the region's formation conditions. We present photoclinometry profiles across these ridges and troughs, which indicate that they are periodic, low-slope features with dominant wavelengths of 3 to 4 km and amplitudes between 100 and 400 m. The morphology of these terrains is consistent with formation via unstable extension of the lithosphere. Our numerical modeling demonstrates that unstable extension can generate large-scale topography under Enceladus-like conditions. Comparison of our photoclinometry profiles with the dominant wavelengths produced by our numerical model permits estimation of the background heat flow at the time the Sarandib–Diyar province formed. We estimate heat flows of 110 to 220 mW m^{-2}, suggesting that resurfacing of the planitiae was accompanied by strong, localized heating. The extension necessary to produce the ridges and troughs may have been caused by now-inactive diapirs, internal phase changes, or other mechanisms. Our heat flux estimates imply elastic thickness at the time of resurfacing of 0.4 to 1.4 km, which are sufficient to have allowed satellite reorientation if the province was underlain by a low-density region. It is therefore plausible that Enceladus has experienced multiple heating events, each leading to localized resurfacing and global reorientation.

Keywords: Enceladus; Satellites, surfaces; Tectonics

1. Background

Saturn's moon Enceladus is one of the great enigmas of the outer Solar System. Its icy lithosphere bears witness to a long history of deformation, creating a surface that spans one of the broadest age ranges in the Solar System: from nearly primordial (4.2 Ga) to perhaps less than one million years old (Plescia and Boyce, 1983; Porco et al., 2006). The variability in surface age is due to regional resurfacing caused by some combination of viscous relaxation of impact craters, cryovolcanism, and tectonic resurfacing (Passey, 1983; Squyres et al., 1983; Kargel and Pozio, 1996). Although it has an effective radius of only 251 km, the satellite is geologically active (Porco et al., 2006; Spencer et al., 2006). This activity is focused in the South Polar Terrain (SPT), which consists of young, tectonically disrupted terrain that is separated from the rest of Enceladus by a sinuous escarpment hundreds of meters high (Porco et al., 2006). The region is further marked by prominent, long, parallel fractures known as "tiger stripes" (Porco et al., 2006), high heat flow (Spencer et al., 2006) and a water ice plume (Hansen et al., 2006; Porco et al., 2006). The geologic activity in the SPT is likely driven by tidal heating resulting from resonant interactions in the saturnian system (Yoder, 1979; Squyres et al., 1983; Lissauer et al., 1984; Ross and Schubert, 1989; Wisdom, 2004), though the specific mechanism remains unclear (Meyer and Wisdom, 2007).

There are several plausible mechanisms capable of creating Enceladus' SPT. One possibility is that the thermal activity and young surface age at the south pole is the result of a low-density diapir in Enceladus' ice or silicate mantle (Nimmo and Pappalardo, 2006). The rise of such a diapir can generate substantial extensional stress within the lithosphere (Janes and Melosh, 1988; Nimmo and Pappalardo, 2006), contributing to the tectonic resurfacing of the region and the creation of the tiger stripe

* Corresponding author. Fax: +1 (520) 621 4933.
E-mail address: mbland@lpl.arizona.edu (M.T. Bland).

0019-1035/$ – see front matter
doi:10.1016/j.icarus.2007.06.011

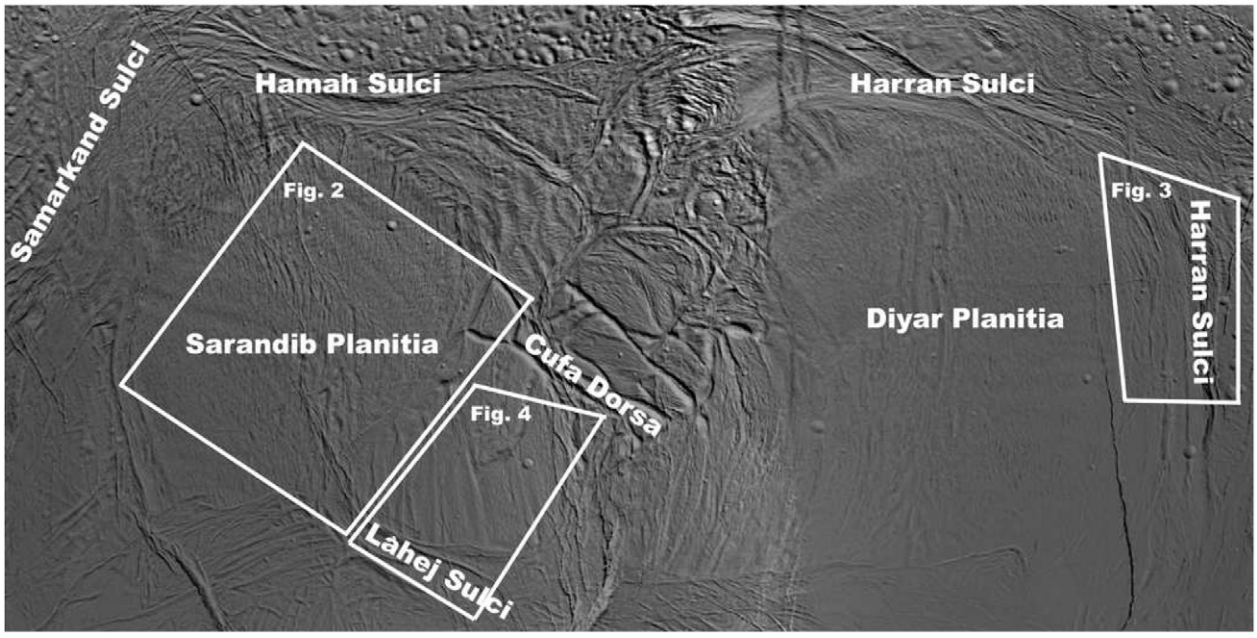

Fig. 1. Cassini and Voyager image mosaic of Enceladus' equatorial region from longitude 225° to 330° W and latitude 20° S to 35° N. The region is marked by the young terrains of Sarandib and Diyar Planitia which are separated from Enceladus' older terrains by a near-continuous chain of Sulcus. The Planitia themselves contain extensive sets of ridges and troughs. White polygonal boxes indicate the approximate location of Figs. 2, 3, and 4. Illumination angle varies across the image but is generally from the southwest. Image courtesy of NASA/JPL-Caltech.

fractures. An additional consequence of a low-density diapir is the reorientation of the satellite such that the density anomaly rotates towards the spin axis. This may explain why Enceladus' active region is centered on the pole (Nimmo and Pappalardo, 2006). Nimmo and Pappalardo (2006) showed that an ice diapir with a sufficient density contrast can cause up to 30° of poleward rotation if the elastic thickness exceeds 0.5 km. Collins and Goodman (2007) have also suggested that tectonic stress and global reorientation can be caused by localized melting within the ice mantle. This mechanism is not only consistent with the high heat flows observed in the SPT, but can also explain the anomalous shape of Enceladus (Collins and Goodman, 2007).

Somewhat older terrains (Sarandib and Diyar Planitia) with a similar geometry and scale to the SPT have also been observed in Enceladus' equatorial region (Helfenstein et al., 2006) (Fig. 1). These young terrains are set apart from the rest of Enceladus by large tectonic structures: Samarkand Sulcus to the west, Hamah Sulcus to the north, and Harran Sulcus to the east. While no tiger stripe like fractures are evident, extensive sets of parallel, north–south trending ridges and troughs occur within the planitiae themselves, and evidence for resurfacing and extensional tectonics abounds.

The ridges and troughs observed in the Sarandib–Diyar province can be formed by a variety of mechanisms (Pappalardo and Greeley, 1995). One such mechanism is unstable extension (also known as extensional necking) of the lithosphere. This mechanism assumes that the lithosphere consists of a brittle surface layer underlain by a viscous substrate. When such a lithosphere extends it can become unstable, causing perturbations in the thickness of the brittle layer to amplify, deforming the surface into parallel, periodically spaced, undulating pinches and swells (Fletcher and Hallet, 1983). Because the ridges and troughs of Ganymede's grooved terrain (the archetypical example of ridge and trough terrain) are periodically spaced (Grimm and Squyres, 1985; Patel et al., 1999), and gently undulating [average slopes are ∼6° (Squyres, 1981)], unstable extension has become the favored mechanism for their formation (e.g., Herrick and Stevenson, 1990; Pappalardo et al., 1998; Collins et al., 1998; Dombard and McKinnon, 2001; Bland and Showman, 2007). Furthermore, it has been suggested that unstable extension may be responsible for ridge and trough terrains throughout the icy satellites (Herrick and Stevenson, 1990).

Semi-analytical, linearized, infinitesimal strain models of unstable extension have found that, assuming a constant growth rate (defined below) and background strain rate, the amplitude of a topographic perturbation in an otherwise uniform flow changes exponentially with the form

$$\mathcal{A} = \mathcal{A}_0 \exp\big[(q-1)\dot{\varepsilon}t\big], \tag{1}$$

where $\mathcal{A}$ is the amplitude of the surface deformation, $\mathcal{A}_0$ is the amplitude of the initial perturbation, q is the exponential growth rate, and $\dot{\varepsilon}t$ is the strain (Fletcher and Hallet, 1983). The growth rate q determines the rate at which topographic amplitudes change under infinitesimal strain. For $q > 1$, the initial perturbation amplifies and extension occurs unstably. While multiple wavelengths may be present in the initial perturbation, the analysis assumes that each wavelength component amplifies independently from the rest, allowing the growth rate of each component to be calculated separately.

Production of large-scale topography, such as the ridges and troughs of the Sarandib–Diyar province, requires high exponential growth rates; adopting a topographic amplification ($\mathcal{A}/\mathcal{A}_0$)

of 10–100 after 10% strain implies that growth rates must achieve ∼40 (Fletcher and Hallet, 1983; Herrick and Stevenson, 1990). Herrick and Stevenson (1990) applied an analytical, infinitesimal strain model of unstable extension to Enceladus and found that exponential growth rates were great enough (⩾40) to produce ridges and troughs several hundred meters high under a broad range of strain rates and lithospheric thermal gradients. The highest growth rates ($q \sim 100$) occurred at high thermal gradients ($>30\ \mathrm{K\,km^{-1}}$) and moderate strain rates ($\sim 10^{-13}\ \mathrm{s^{-1}}$). Subsequent work has shown that the inclusion of grain-size-sensitive flow laws for ice, such as grain boundary sliding (GBS) [not included in Herrick and Stevenson (1990)], act to further increase instability growth rates (Dombard and McKinnon, 2001). Thus, based on these analyses, unstable extension could have produced much of Enceladus' periodic ridges and troughs.

Numerical modeling of unstable extension has shown, however, that as extension progresses to finite strains (>5%), growth does not continue exponentially [as predicted by Eq. (1)] but decreases rapidly, limiting the total amplitude of the deformation produced by extension (Bland and Showman, 2007). Furthermore, numerical modeling has also shown that the use of a more realistic plastic rheology and the inclusion of elastic behavior produces exponential growth rates an order of magnitude lower than those calculated by the linearized perturbation model described above (Bland and Showman, 2007). These low growth rates further limit the total amount of amplification produced by extension. Because of these difficulties, the applicability of unstable extension to the formation of Enceladus' ridge and trough terrains must be reassessed.

A salient feature of unstable extension is that the morphology (wavelength and peak to trough amplitude) of the deformation produced depends sensitively on the thermal gradient of the lithosphere (Fletcher and Hallet, 1983). In general, a specific wavelength component amplifies significantly faster (has much larger q) than the other wavelengths, producing strongly periodic topography. High thermal gradients produce short wavelength topography while low thermal gradients produce long wavelength topography. Comparison between measurements of topographic wavelengths within ridge and trough terrains and models of extensional necking therefore permits estimation of the thermal conditions in the lithosphere during ridge and trough formation (Fink and Fletcher, 1981; Dombard and McKinnon, 2001).

In this paper we first describe new measurements of ridge and trough topography within the Sarandib–Diyar province derived from photoclinometry profiles (Section 2). We then use a numerical, nonlinear, finite strain model to determine whether unstable extension is applicable to Enceladus (Section 3). We find that, under certain conditions, instability growth is strong enough to have produced the ridges and troughs of the Sarandib–Diyar province (Section 4). Comparison of the dominant wavelengths produced by the numerical model to our topographic profiles allows estimation of the thermal gradient and elastic thickness of the lithosphere during the extensional event (Section 5).

2. Photoclinometry

2.1. Method

In order to obtain an estimate of the topography of the ridge and trough terrain, we use a profiling photoclinometry technique based upon the point photoclinometry technique of Beyer et al. (2003). This technique provides a model slope for an individual pixel. By taking a profile of such pixels in the down-Sun direction, a topographic profile can be constructed.

The method uses a lunar-Lambert photometric function of the form (Beyer et al., 2003)

$$I(\mu, \mu_0, \alpha) = B_0(\alpha)\left[\frac{2L(\alpha)\mu_0}{\mu + \mu_0} + \big(1 - L(\alpha)\big)\mu_0\right], \tag{2}$$

where $I(\mu, \mu_0, \alpha)$ is the reflectance function, μ is the cosine of the emission angle, μ_0 is the cosine of the incidence angle, α is the phase angle, $B_0(\alpha)$ is the intrinsic albedo, and $L(\alpha)$ is a function of the photometric properties of Enceladus' surface and is given by McEwen (1991). To calculate $L(\alpha)$ we use photometric properties derived from Voyager and ground based observations of Enceladus' surface (Verbiscer and Veverka, 1994): width parameter for the opposition effect (h) of 0.05 (Hapke, 1986), opposition surge amplitude (B_0) of 0.21, single-scattering albedo (w) of 0.998, macroscopic roughness parameter ($\bar{\theta}$) of 6°, and a Henyey–Greenstein asymmetry parameter (g) of −3.999 (Verbiscer and Veverka, 1994). While these parameters are uncertain, determination of model slope values is robust to small variations in the value of L (Beyer et al., 2003). The parameters listed above and the various phase angles of the profiles led to different values of L that were used for each image. They varied from 0.13 to 0.23.

When a profile of pixels is taken in the down-Sun direction, the average brightness of those pixels (I) is assumed to be the brightness of a flat surface. The brightness of each individual pixel (I^*) is then divided by the flat brightness. Because the incidence and emission angles of the flat surface are known from the spacecraft geometry, use of the ratio of I^*/I permits determination of the slope of an individual pixel (θ) relative to the flat surface. This study uses the same table-lookup mechanism quantized to the quarter degree in θ as described in Beyer et al. (2003). All Cassini ISS images (Porco et al., 2004, 2005b) were first processed with CISSCAL 3.3 (Porco et al., 2005a) and then imported into ISIS 2 (Gaddis et al., 1997; USGS, 2007) to obtain estimates of the photometric angles and image geometry.

The point photoclinometry method returns a slope for each pixel. To convert that slope into a change in elevation across that pixel, the width of the pixel in distance units as well as the down-Sun direction (equivalent to the profile direction) must be known. We choose not to geometrically reproject the images that we used. While doing so would alleviate some sources of error, it would also introduce others. The pixels we measured did not represent a square area on the surface of Enceladus, but instead a rectangle (different resolution in the line and sample directions). Since we are only interested in the length of the

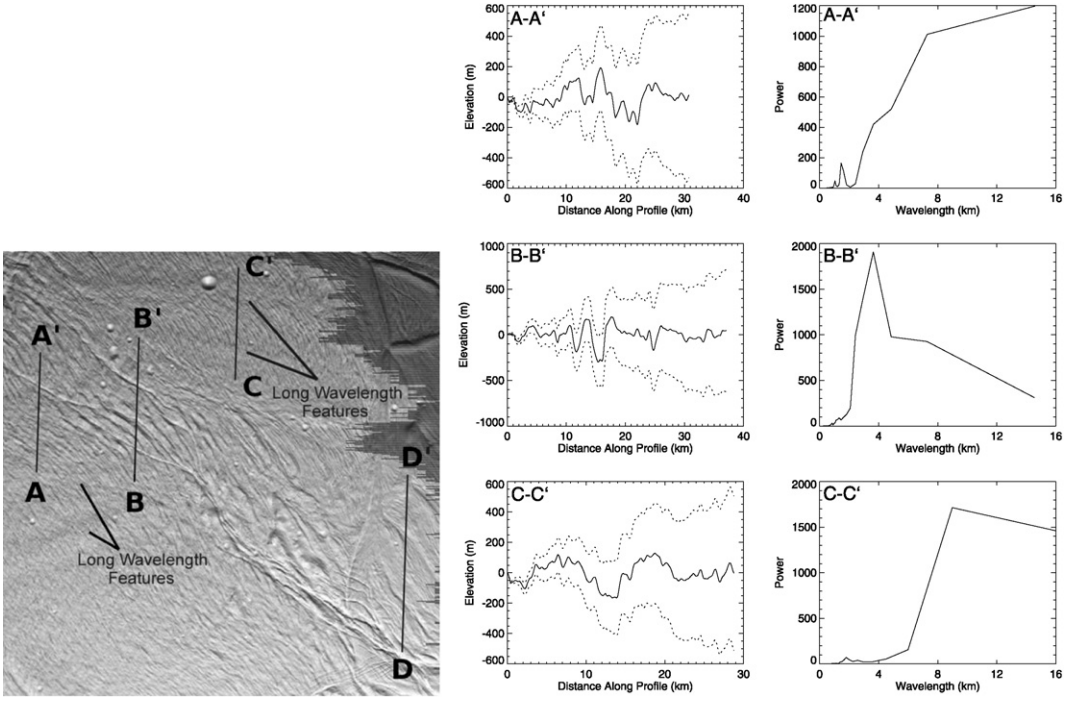

Fig. 2. Portion of Cassini ISS image N1487300285_1 of Sarandib Planitia with photoclinometry profiles and Fourier spectra. In the profiles, solid lines indicate the measured topography and dotted lines indicate the $\pm 1^\circ$ error envelope. Spectra show geometrically corrected wavelengths. The topography and power spectrum of profile DD′ is shown in Fig. 4. The long-wavelength features indicated in the image run approximately southwest to northwest near profiles AA′ and BB′ and approximately west–northwest to east–southeast near profile CC′. They show up as broad albedo features with a wavelength of ∼10 km. Profiles AA′, BB′, and CC′ are 30.7, 37.0, and 28.8 km long, respectively.

profile segment, x, that runs through a given pixel in the down-Sun direction, we assume that the resolution of that pixel, r, is that of the resolution of the axis closest in direction (vertical or horizontal) to the strike of the profile direction. The profiles on the images in this study are mostly vertical, so the value of r was taken from the line resolution. We define ψ as the angle between the profile direction and pixel axis, where $0^\circ \leqslant \psi \leqslant 45^\circ$. We calculate the distance, x, across each pixel along the profile as

$$x = \frac{r}{\cos\psi}. \tag{3}$$

We make the simplifying assumption that ψ and r, hence x, do not change across the profile so Eq. (3) is evaluated only once for each profile.

Once the distance across each pixel, x, is obtained from Eq. (3), the elevation difference, Δz, can be determined across each pixel. If a given pixel has a angle, θ [derived from the Beyer et al. (2003) technique], then

$$\Delta z = x \tan\theta. \tag{4}$$

The distance and the elevation difference across each pixel can be put together to make a profile of elevation as a function of distance along that profile.

The creation of a topographic profile in this manner is a cumulative process. Unfortunately, the errors are cumulative as well. The error in the elevation across the first pixel depends on the error in the distance across that first pixel, x, and the error in the slope, θ, for that pixel. The error in the elevation after the second pixel is dependent on the errors in x and θ for the second pixel as well as those in the first, and so on. So in addition to the errors inherent in the point photoclinometry technique [e.g., difficulties of albedo variation and slope azimuth (Beyer et al., 2003)], there is the added contribution of this cumulative error for the profiling photoclinometry technique. As a result, the absolute elevation difference between the beginning and end of a profile is not very reliable. However, relative elevation differences are reliable if they are separated by only a few tens of pixel distances.

An additional source of error comes from the fact that the photometric angles are going through significant changes from one end of the profile to another due to Enceladus' planetary curvature (the profiling photoclinometry technique assumes that the profile is on "flat" terrain). This causes the original profiles to have an artificial parabolic shape and contributes error to the amplitude of features in the topography, but does not affect wavelengths.

Finally, because any variation in pixel values are assumed to be due to variations in pixel slope alone, photoclinometry techniques can be strongly affected by shadows. True shadows in the image would cause the photoclinometry algorithm to report erroneously large negative slopes. The incidence angles for the profiles in this study are $35^\circ \pm 5^\circ$, which indicates that there would have to be a true slope steeper than $55^\circ \pm 5^\circ$ to cast such a shadow, and that slope would have to be at least 125 m tall to completely shadow one pixel in the highest resolution image in this study (88 m/pixel). While landforms of this size are unlikely, they are not impossible. We carefully exam-

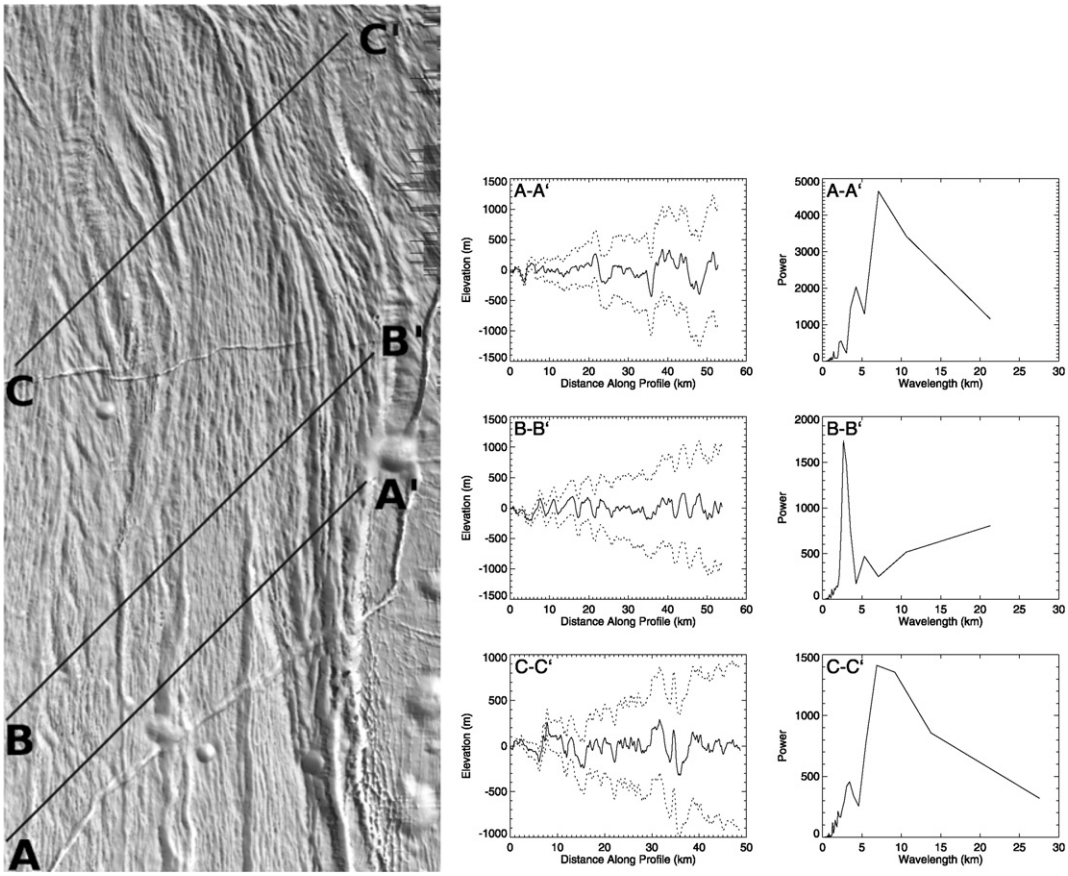

Fig. 3. Portion of Cassini ISS image N1489049936_2 of Diyar Planitia with photoclinometry profiles and Fourier spectra. In the profiles, solid lines indicate the measured topography and dotted lines indicate the $\pm 1^\circ$ error envelope. Spectra show geometrically corrected wavelengths. Profiles AA′, BB′, and CC′ are 52.8, 53.9, and 48.7 km long, respectively.

ined the model slopes produced by the algorithm for all profiles, and found no slopes greater than 45°. Although a true slope of $55^\circ \pm 5^\circ$ would cast a shadow, the model slope reported by the photoclinometry algorithm for such a shadowed pixel would be much greater. Therefore, we do not believe that our results are affected by the presence of shadows.

2.2. Topography

Photoclinometry profiles were obtained within Sarandib Planitia, Diyar Planitia, and the region between the two Planitiae, bounded to the north by Cufa Dorsa and to the south by Láhej Sulcus (hence forth referred to as the Cufa–Láhej region) (Fig. 1). To determine whether the ridge and trough terrain is periodic, a Fourier analysis was performed on each profile. This analysis required that the parabolic shape of the profiles be removed. This was accomplished by fitting, and subsequently subtracting off a 3rd or 4th order polynomial from each profile, creating a "flattened" version of the topography. Because the topographic wavelengths of interest are much shorter than the long-wavelength artifact, and because subtraction of the polynomial fit has no affect on the wavelengths present within the terrain, the following results are independent of the details of the polynomial fit (e.g., order or y-intercept). With the long-wavelength artifact removed, the profile was Fourier transformed to search for periodicity. Because photoclinometry profiles were taken in the down-Sun direction rather than perpendicular to the ridges and troughs, the wavelengths determined from the Fourier analysis as well as topographic amplitudes required geometric correction. Furthermore, the Fourier method we used returns power values at constant interval wavenumbers (km^{-1}). The spectral resolution in kilometers is therefore not constant but decreases at long wavelengths. This has the affect of smearing out the long wavelength information contained in the spectra. The "flattened" profiles and their Fourier spectra are shown in Figs. 2, 3, and 4.

Three photoclinometry profiles were constructed within Sarandib Planitia (Fig. 2). Profile BB′ indicates that the ridges and troughs of Sarandib have a strong periodicity with a wavelength of ∼4 km. The dominant features in this profile have amplitudes of ∼400 m, while the smaller ridges and troughs have amplitudes of 100–200 m. Profile CC′ indicates that longer wavelength deformation (8 to 10 km) also occurs within Sarandib. This gently undulating deformation (the average slope in profile CC′ is 6°) is oriented roughly east to west, diagonal to the dominant northwest–southeast trend of the shorter wavelength ridges and troughs in profile BB′. These features have amplitudes of ∼200 m. Similar undulations can be seen just to the south of profiles AA′ and BB′. Profile AA′ shows no obvious moderate wavelength ($\geqslant$2 km) periodicity, though long

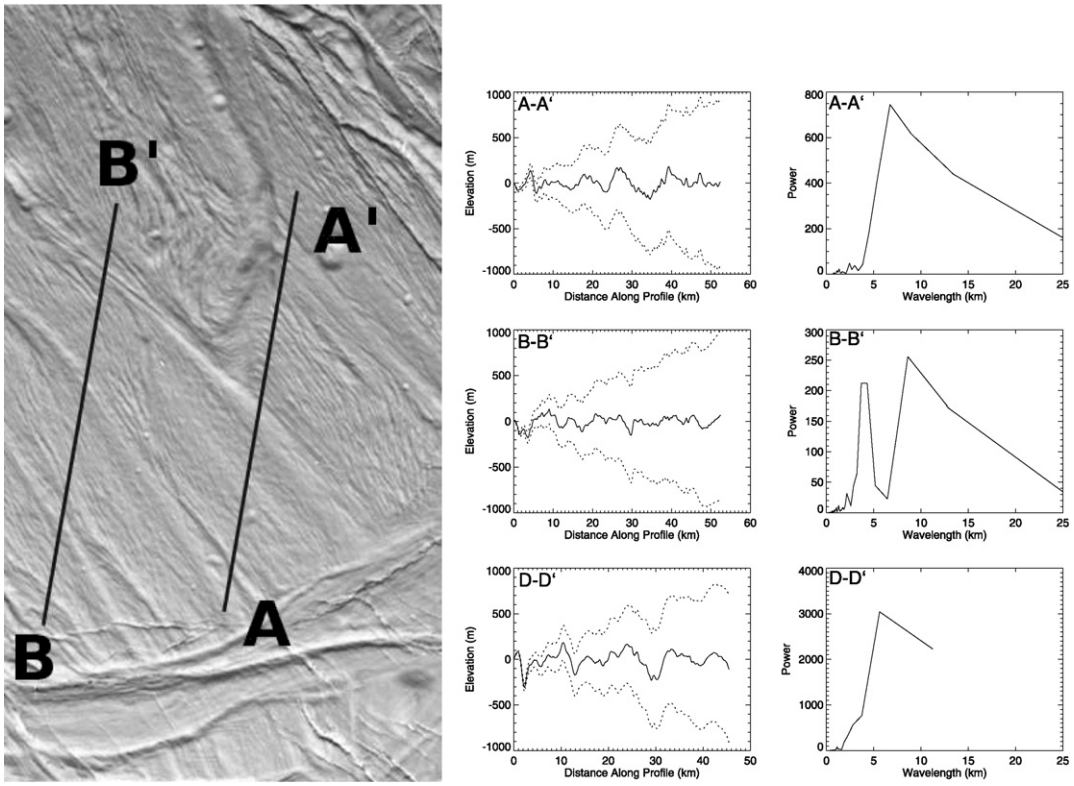

Fig. 4. Portion of Cassini ISS image N1487300107_1 of the Cufa–Láhej region with photoclinometry profiles and Fourier spectra. In the profiles, solid lines indicate the measured topography and dotted lines indicate the ±1° error envelope. Spectra show geometrically corrected wavelengths. The location of profile DD′, on the northwest edge of the Cufa–Láhej region, is shown in Fig. 2. Profiles AA′, BB′, and DD′ are 52.4, 52.4, and 45.5 km long, respectively.

wavelengths are clearly present in the spectrum. A weak peak at 1.5 km is observed, suggesting a fine scale tectonic fabric in the region. This fabric is also evident in the power spectra of profile BB′ and CC′ but tends to be washed out by the strong peaks at other wavelengths. We conclude that this tectonic fabric pervades the Sarandib Planitia region. Average (RMS) slopes in the Sarandib Planitia profiles are between 6° and 10°. Finally, we note that the low angles between the down-Sun direction and visually dominant northwest–southeast trending ridges and troughs makes accurate characterization of their true amplitudes and wavelengths difficult.

Despite their apparent diversity, the three profiles paint a coherent picture of complex extensional deformation within Sarandib Planitia. Profile BB′, which shows strong periodicity, transects a swath of large-amplitude, periodically-spaced ridges and troughs. These are the dominant tectonic features in the region. However, the amplitude of these features decreases to the west, until they are unobservable in profile AA′. This pattern suggests that the amount of strain (and thus amplitude of the topography produced) varied locally within the planitia during the extensional event. Long wavelength deformation (profile CC′) trending diagonally to the dominant northwest–southeast ridges and troughs may be the result of overprinting, wherein deformation of one wavelength has formed on, but not completely destroyed, older deformation of a different wavelength.

Diyar Planitia bears a strong resemblance to Sarandib Planitia, with numerous parallel ridges and troughs oriented in the north–south direction (Fig. 3). Each of the three profiles constructed contains at least two deformation wavelengths. The power spectrum of Profile AA′ reveals a broad peak at 7.1 km and a smaller but significant peak at 4.3 km. This weaker peak appears to be associated with finer-scale ridges and troughs, similar in appearance to those of Sarandib Planitia, while the peak at 7.1 km appears related to the spacing of several large-amplitude graben-like features. Amplitudes within this profile are generally 300 to 400 m, the highest of any ridged terrain we examined. The ridges and troughs of Profile BB′, just north of profile AA′, are strongly periodic with a wavelength of 2.7 km. A second, weaker peak at 5.4 km is also present. Topographic amplitudes in this region are 200 to 300 m. Profile BB′ appears to transects fewer large scale features and thus seems to provide a relatively uncomplicated profile of the ridge and trough topography of Diyar Planitia. Like profile AA′, profile CC′ in the northern reaches of Diyar Planitia contains a broad wavelength peak at 7 km and weaker but significant peak at 3.5 km. Again, the shorter wavelength peak appears related to ridge and trough terrain while the long wavelength peak results from the spacing of several-large amplitude features. Amplitudes within this profile approach 300 m. Finally we note that near the image resolution limit, finer scale deformation occurs. This deformation appears in the power spectra as a very weak signal at short wavelengths, and is likely associated with small-scale faulting that accommodates the large-scale deformation. Average slopes in Diyar Planitia are 12° to 13°, somewhat higher than in Sarandib Planitia.

We conclude that Diyar Planitia contains periodically spaced ridges and trough with wavelengths between 2.7 and 4 km. The Fourier spectra of each profile indicates a significant peak within this wavelength range. Superimposed on these ridges and trough are several large, long-wavelength features. Because these features have larger amplitudes than the shorter wavelength ridges and troughs, their spacing produces strong peaks in the power spectra. Finally, like Sarandib Planitia, short wavelength deformation may be accommodating the long-wavelength topography. While the geologic picture is complex, the appearance of multiple scales of deformation, including the coexistence of ridges-and-troughs and graben, is consistent with high resolutions images of grooved terrain on Ganymede (Pappalardo et al., 1998).

The Cufa–Láhej region also contains regularly spaced, parallel grooves trending northwest–southeast. Topographic wavelengths within this region have peaks between 4 and 9 km with amplitudes of ∼100 m (Fig. 4). Comparison to the image (Fig. 4) suggests that the long-wavelength undulatory features (6–10 km) dominate the topography. These low amplitude features have average slopes between 5° and 7° and are reminiscent of the gently undulating east-west trending features in Sarandib Planitia (Fig. 2, profile CC′). The power spectrum of profile BB′ indicates that two wavelengths are present in the deformation, one at 4 km and one at 8.5 km, suggesting a complex history of extension. Several shorter wavelengths between 1 and 2.5 km are also present in the region. These short wavelength features are consistent with the tectonic fabric seen throughout Sarandib–Diyar province.

Several characterizations of the "typical" ridge and trough morphology found in the Sarandib–Diyar province may be made. Both Sarandib and Diyar Planitia contain northwest–southeast or north–south trending quasi-periodic ridges and troughs with wavelengths near 3 to 4 km. The Cufa–Láhej region contains longer wavelength deformation with dominant wavelengths of 4 to 9 km. Long-wavelength deformation is also present in both planitiae and suggests a complex history of tectonism in the region. Average slopes throughout the Sarandib–Diyar province are 5° to 13° with maximum slopes up to 45°. This indicates that, while there are exceptions, the ridges and troughs in the region are mostly low-slope features. Short wavelength (generally 1 to 2 km) deformation occurs throughout the entire Sarandib–Diyar Planitia and may be the result of small-scale fracturing that is accommodating the large-scale deformation (Pappalardo et al., 1998). These observations suggest that the ridges and troughs in the Sarandib–Diyar province consist of parallel, periodically spaced structures with low slopes and are therefore consistent with formation via unstable extension of the lithosphere.

3. Numerical modeling of unstable extension

In order to determine whether the ridges and troughs of the Sarandib–Diyar province are consistent with unstable extension, the necking instability mechanism must be reassessed under Enceladus-like conditions. Following the methods of Bland and Showman (2007), we use the Lagrangian, finite-element model TEKTON (version 2.3) in plane strain (Melosh and Raefsky, 1980) to examine the growth of instabilities during extension of an icy lithosphere as a function of strain rate and vertical temperature gradient. The model incorporates elastic, power-law viscous, and plastic rheologies appropriate to an Ice I layer such that the total strain rate is given by

$$\dot{\varepsilon}_{\text{total}} = \dot{\varepsilon}_{\text{elastic}} + \dot{\varepsilon}_{\text{visco}} + \dot{\varepsilon}_{\text{plastic}}, \tag{5}$$

where $\dot{\varepsilon}_{\text{elastic}}$, $\dot{\varepsilon}_{\text{visco}}$, and $\dot{\varepsilon}_{\text{plastic}}$ refer to the elastic, viscous, and plastic strain rates, respectively. The viscous strain rate utilizes a composite flow law with the form (Goldsby and Kohlstedt, 2001)

$$\dot{\varepsilon}_{\text{visco}} = \dot{\varepsilon}_{\text{A}} + \dot{\varepsilon}_{\text{B}} + \dot{\varepsilon}_{\text{C}} + \dot{\varepsilon}_{\text{diff}} + \{1/\dot{\varepsilon}_{\text{GBS}} + 1/\dot{\varepsilon}_{\text{BS}}\}^{-1}, \tag{6}$$

where the subscripts A, B, C, diff, GBS, and BS refer to dislocation creep A, B, and C; diffusion creep; grain boundary sliding; and basal slip. Each of these mechanisms has a temperature and stress dependence of the form:

$$\dot{\varepsilon} = A(1/d)^m \acute{\sigma}^n \exp\{-Q/RT\}, \tag{7}$$

where $\dot{\varepsilon}$ and $\acute{\sigma}$ are the effective strain rate and deviatoric stress, respectively, A is a mechanism dependent constant, d is the grain size, m is the grain size exponent, n is the power-law exponent, Q is the activation energy, R is the gas constant, and T is the absolute temperature. The relevant rheological parameters are shown in Table 1. Because the values of A_{ex} given in Table 1 are determined in uniaxial stress experiments, they must be multiplied by a correction factor such that $A = (3^{(n+1)/2}/2)A_{\text{ex}}$ before they can be applied to Eq. (7) (Ranalli, 1995, p. 77). This factor was not included in these simulations, but its effect is generally smaller than other uncertain parameters (e.g., grain size, surface yield stress) (Bland and Showman, 2007). We used a grain size of 1 mm in all simulations.

Table 1
Rheological parameters

Creep regime	$\log A_{\text{ex}}$ ($\text{MPa}^{-n}\,\text{m}^{m}\,\text{s}^{-1}$)	m	n	Q (kJ mol^{-1})	Reference
Dislocation creep					
Regime A	11.8	0	4.0	91	Kirby et al. (1987)
Regime B	5.1	0	4.0	61	Kirby et al. (1987)
Regime C	−3.8	0	6.0	39	Durham et al. (1997)
GBS	−2.4	1.4	1.8	49	Goldsby and Kohlstedt (2001)
BS	7.74	0	2.4	60	Goldsby and Kohlstedt (2001)
Volume diffusion	−3.46	2	1.0	59.4	Goldsby and Kohlstedt (2001), Barr and Pappalardo (2005)

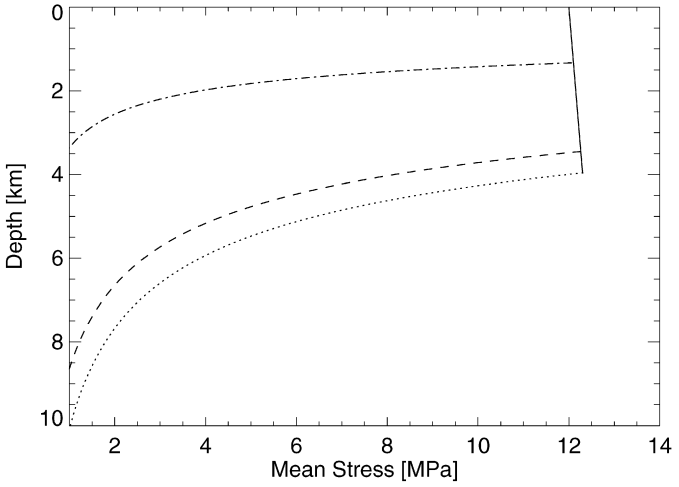

Fig. 5. Model strength envelops in Enceladus' initial lithosphere for three cases: $\dot{\varepsilon} = 10^{-13}$ s^{-1}, $dT/dz = 15$ K km^{-1} (dotted); $\dot{\varepsilon} = 10^{-14}$ s^{-1}, $dT/dz = 15$ K km^{-1} (dashed); $\dot{\varepsilon} = 10^{-13}$ s^{-1}, $dT/dz = 45$ K km^{-1} (dot–dash). Because of Enceladus' low gravity, the frictional yield stress (solid line) has only a small increase with depth.

Plasticity, a continuum mechanics formulation of brittle behavior, is incorporated into the model via Drucker–Prager yielding, which has a yield condition with the form

$$\sigma_{\text{yield}} = \xi(C\cos\phi - \sigma_m \sin\phi), \tag{8}$$

where C is the cohesion, ϕ is the angle of internal friction, σ_m is the mean stress (negative in compression), and $\xi = 6/[\sqrt{3}(3 - \sin\phi)]$. We use a cohesion value of 10 MPa and an angle of internal friction of 30° to define the strength profile of the lithosphere as

$$\sigma_{\text{yield}} = 12\ \text{MPa} - 0.69\sigma_m. \tag{9}$$

This formulation produces a yield stress that increases with depth in accordance with Byerlee's law; however, because of Enceladus' low gravity, the increase in yield strength with depth is small. Typical strength profiles are shown in Fig. 5. We note, however, that the surface yield stress in Eq. (9) is an order of magnitude higher than laboratory yield stresses measured for ice (Beeman et al., 1988). Use of this high value of cohesion allows a simpler examination of how other parameters (i.e. strain rate and temperature gradient) affect unstable extension. Lowering the cohesion can have a strong effect on the amplitude of the simulated deformation; however, dominant wavelengths remain unchanged (Bland and Showman, 2007).

If the second invariant of the deviatoric stress tensor within a finite-element exceeds the yield stress (σ_{yield}) plastic flow initiates and the term $\dot{\varepsilon}_{\text{plastic}}$ in Eq. (5) becomes nonzero, increasing the total strain rate within that element. We emphasize that when and where plastic flow occurs during a simulation is not determined a priori, but depends entirely on the local stress state. This permits plastic flow, and thus higher strain rates, to localize in regions of high stress.

We assume a linear thermal gradient within the lithosphere of Enceladus and investigate temperature gradients ranging from 2 to 45 K km^{-1}. The surface temperature is assumed to be 70 K, consistent with a simple solar equilibrium temperature and, except at the surface, isotherms are initially horizontal. To insure numerical stability, we cut off the temperature increase with depth at 180 K. While done for numerical reasons, the transition from a linear thermal gradient to a constant temperature is consistent with (but colder than) having a thick convecting layer at depth. However, neither convection nor conduction are included in the model. Extensional thinning in the absence of conduction effectively increases the thermal gradient within the lithosphere. This is a reasonable result for models in which the timescale for extension is less than the timescale for thermal diffusion (i.e. simulations with low thermal gradients and high strain rates). However, for simulations with high thermal gradients and low strain rates (i.e. simulations in which thermal diffusion would occur faster than extension) the inclusion of conduction would maintain the original imposed thermal gradient. The lack of conduction in these simulations therefore causes a moderate ($\leqslant$30%) shift in the thermal gradient at which maximum amplification occurs. However, our qualitative results are not affected (Bland and Showman, 2007).

A total extensional strain of 31.5% is applied to the model lithosphere over timescales ranging from 10^4 to 10^7 years. This implies strain rates spanning three orders of magnitude from 10^{-12} to 10^{-15} s^{-1}. The value of strain used is consistent with measurements of truncated craters in Enceladus' northern hemisphere, which suggest several tens of percent strain has occurred (Passey, 1983). Our model domains utilize a cartesian geometry and are 40 to 200 km long, 12 to 96 km deep, and have square elements 167 m to 1 km on a side. Extension is produced by fixing the left boundary of the domain while applying a constant velocity boundary condition to the right side. Both the left and right sides of the domain are free slip in the vertical direction while the bottom boundary is fixed in the vertical and free in the horizontal. A small amplitude (generally 10 m peak to trough), sinusoidal perturbation is applied to the surface of the domain to allow instabilities to initiate.

We apply a constant gravitational acceleration of 0.113 m s^{-2} to the model, which we initialize by letting the stress relax towards a purely hydrostatic state. Due to the cold surface temperatures, a true hydrostatic state is never reached in the upper portion of the domain; however, the effect of this initial deviation is small (Bland and Showman, 2007). The low gravitational acceleration of Enceladus is favorable for instability growth as less work must be performed against gravity to displace material under lithospheric swells (Herrick and Stevenson, 1990).

We monitor the growth of an instability by periodically extracting and Fourier transforming profiles of the surface to create spectra of the deformation. Because instability growth depends strongly on wavelength, we perform a range of simulations with different initial perturbation wavelengths for each combination of temperature gradient and strain rate. This allows determination of both the dominant wavelength and total peak to trough amplification ($\mathcal{A}/\mathcal{A}_0$) produced by extension. We also performed simulations in which the initial perturbation consisted of many (16) superposed wavelength components to assess unstable extension's ability to produce strongly periodic topography from random initial topography. In these simulations each wavelength component was given a random phase

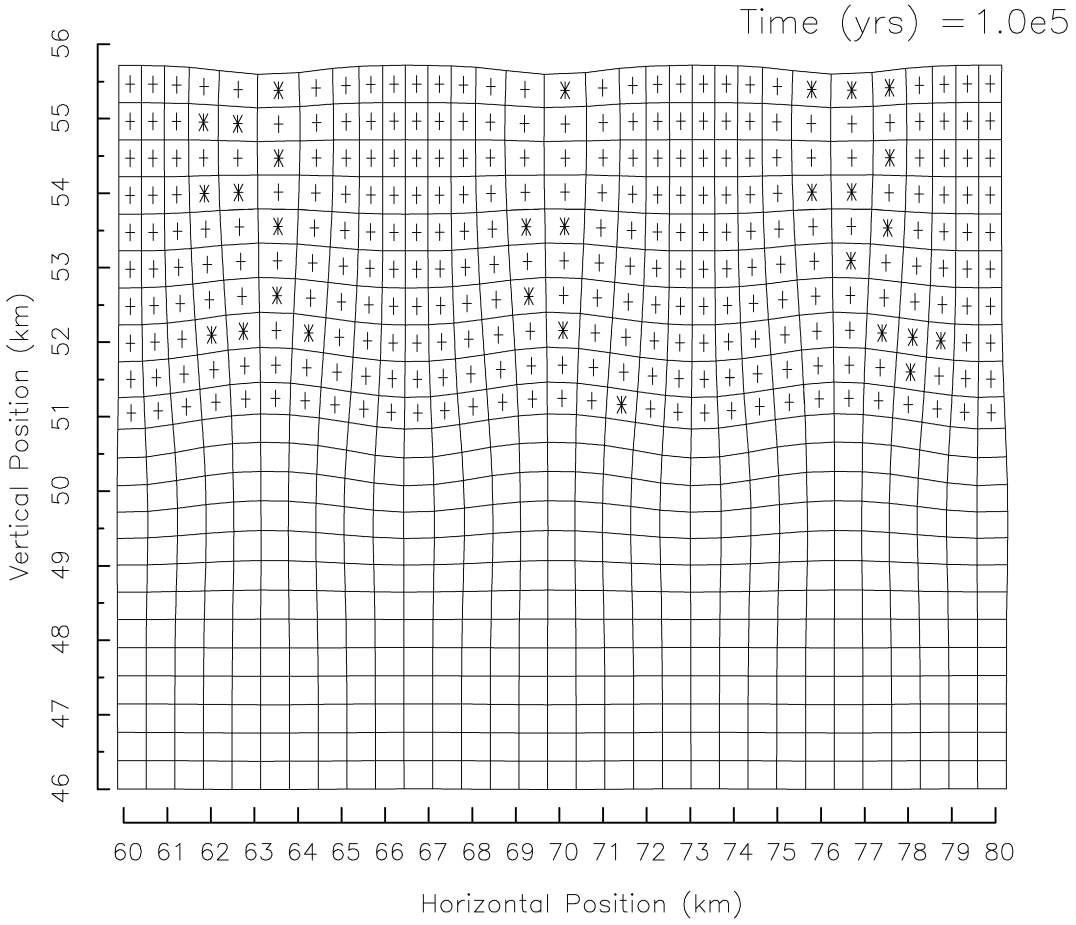

Fig. 6. Portion of a typical output of the finite element model after 31.5% extension showing material contours that were originally horizontal and vertical. Asterisks indicate where plastic flow occurred in the most recent timestep. Plus signs indicate where plastic flow has occurred at some point during the simulation. The scattered distribution of plastic deformation occurring in the most recent timestep (asterisks) is due to plastic failure relaxing stresses back below the criterion for yielding. Several timesteps are required before stresses again exceed this criterion. Thus while the whole layer behaves plastically, only a fraction of the individual elements undergo plastic failure in a given timestep.

shift, added together, and renormalized to have a maximum peak to trough amplitude of 15 m. The simulations were otherwise identical to those described above.

4. Modeling results

Extension of the model domain described above produces moderate amplitude, periodically spaced pinches and swells (Fig. 6). Plastic deformation is limited to the upper portion of the domain where it concentrates within lithospheric pinches. Thus strain is highly focused in the pinched regions with little deformation occurring outside those zones. Tensional stress dominates the near-surface elements within the model, and like the strain, is especially concentrated within pinched regions. At depth, stresses become hydrostatic. These results are consistent with periodic necking occurring during unstable extension of the lithosphere.

The exact form of the surface deformation depends strongly on the thermal gradient and strain rate imposed on the simulation. Fig. 7 shows typical profiles of the surface deformation after 31.5% extension for four simulations. In general, high thermal gradients produced low-amplitude, short-wavelength deformation (57 m amplitude, 2.2 km wavelength in Fig. 7A) and low thermal gradients produced large-amplitude, long wavelength deformation (172 m amplitude, 18.8 km in Fig. 7C).

Fig. 8 shows contours of the total amplification of the initial topography ($\mathcal{A}/\mathcal{A}_0$) and dominant wavelengths as a function of temperature gradient and strain rate after 31.5% strain. Because we have applied finite strain to the model, the strain rate is actually not constant throughout the simulation but decreases by ∼24% as extension occurs. Furthermore, extensional thinning of the lithosphere causes an increase in the vertical thermal gradient during extension. Thus, the strain rates and temperature gradients shown in Fig. 8 indicate the initial values for each simulation. The maximum amplification (19.2) occurs at moderate strain rates ($10^{-13}\,\mathrm{s}^{-1}$) and low thermal gradients (2 to 5 $\mathrm{K\,km}^{-1}$). This amplification means that 10 m of initial topography was amplified to 192 m after 31.5% extension. Total amplification falls off rapidly with increasing strain rate and more moderately with decreasing strain rate. This dependence on strain rate is consistent with the results of Herrick and Stevenson (1990) and Dombard and McKinnon (2001), and occurs because the strength contrast between the lithosphere and

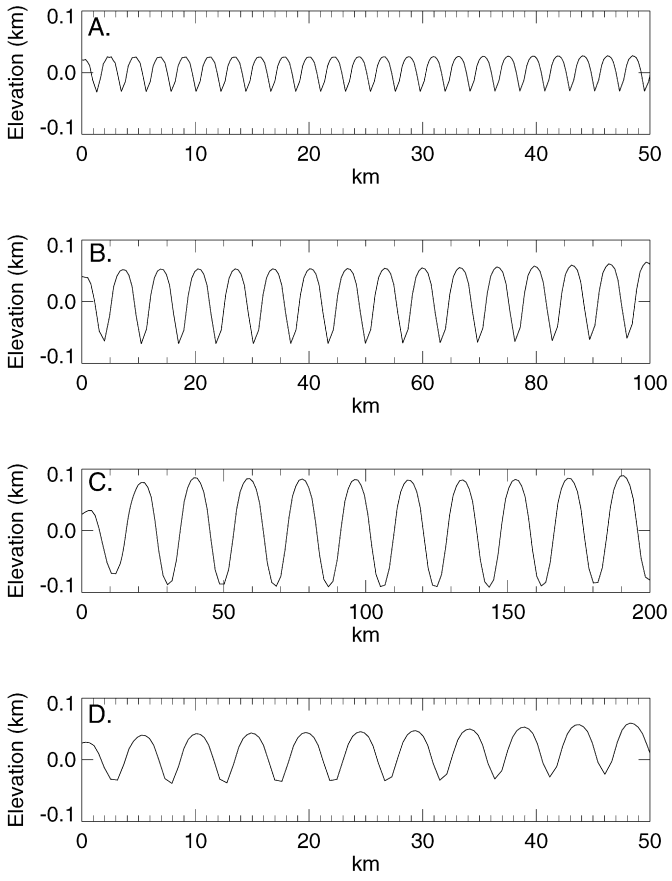

Fig. 7. Typical profiles of the surface deformation produced after 31.5%. Each simulation was initialized with a 10 m sinusoidal perturbation with a wavelength equal to the dominant wavelength. The final surface deformation depends heavily on both the strain rate and the vertical thermal gradient imposed. (A) $\dot{\varepsilon} = 10^{-13}$ s^{-1}, $dT/dz = 45$ K km^{-1}. (B) $\dot{\varepsilon} = 10^{-13}$ s^{-1}, $dT/dz = 15$ K km^{-1}. (C) $\dot{\varepsilon} = 10^{-13}$ s^{-1}, $dT/dz = 5$ K km^{-1}. (D) $\dot{\varepsilon} = 10^{-15}$ s^{-1}, $dT/dz = 15$ K km^{-1}.

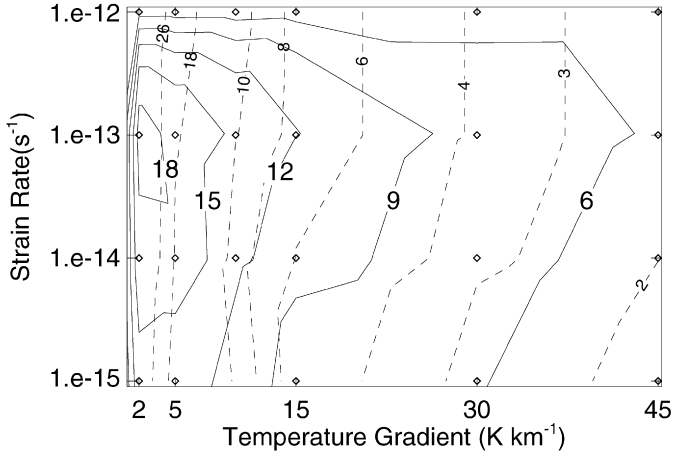

Fig. 8. Contours of total amplification ($\mathcal{A}/\mathcal{A}_0$) (solid) and dominant wavelengths in km (dashed) after 31.5% strain as a function of strain rate and thermal gradient. Amplification is a maximum for moderate strain rates (10^{-13} s^{-1}) and low thermal gradients (2 K km^{-1}). Each simulation was initialized with a single 10-m amplitude, sinusoidal perturbation at the dominant wavelength. Diamonds indicate parameter values used for the simulations.

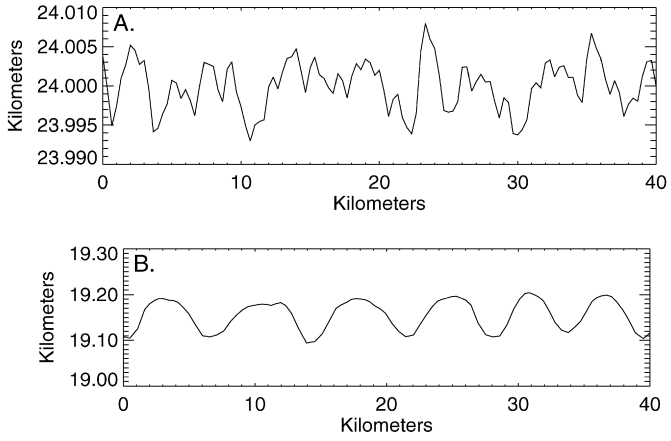

Fig. 9. Surface profiles of (A) the initial perturbation and (B) the final deformation after 31.5% extension for a simulation with a strain rate of 10^{-13} s^{-1} and thermal gradient of 15 K km^{-1}. The initial perturbation is composed of 16 sinusoids of different wavelength, each given a random phase shift, added together, and renormalized to have a maximum peak to trough amplitude of 15 m. A single wavelength of the initial perturbation amplifies faster than all others, producing large amplitude, periodic pinches and swells in the final deformation. Note that in (B) only 40 km of the 52-km extended final domain are shown to allow direction comparison to (A).

substrate is a peaked function of the strain rate and thus has a maximum at some value (Herrick and Stevenson, 1990).

Despite the large amplification occurring at low thermal gradients, amplification does approach zero as the thermal gradient approaches zero (as expected). Total amplification also decreases with increasing temperature gradient, being a factor of three lower at 45 K km^{-1} than at 2 K km^{-1}. This decrease is not predicted by an extrapolation of exponential growth rates derived from analytical models and results from nonlinear processes at large strains (Bland and Showman, 2007).

Minimum dominant wavelengths (1.6 km) occur at high thermal gradients (45 K km^{-1}) and low strain rates (10^{-15} s^{-1}). Wavelengths increase nonlinearly with decreasing thermal gradient with a maximum of 37.6 km at low thermal gradients (2 K km^{-1}) and high strain rates (10^{-12} s^{-1}). Dominant wavelengths depend only weakly on strain rate, with higher strain rates producing slightly longer wavelengths for a given thermal gradient.

Finite extension (31.5%) of a domain with multiple wavelength components in the initial perturbation (Fig. 9A) leads to the development of periodic structures in the final surface deformation (Fig. 9B). As in the simulations with a single sinusoidal perturbation, the amplitude and dominant wavelength of final surface deformation depends strongly on the imposed vertical thermal gradient: high thermal gradients produce short wavelength deformation and low thermal gradients produce long wavelength deformation. The final surface deformation does not depend on the exact form of the initial topography, only on the wavelengths present. Thus, changing the random phase shift given to each wavelength component in the initial condition changes the appearance of the initial topography but does not affect the final deformation.

The inclusion of multiple wavelengths of topography in the initial perturbation affects the resulting deformation in two

ways. First, the total amplification decreases moderately. A simulation with a strain rate of $10^{-13}\,s^{-1}$, thermal gradient of $15\,K\,km^{-1}$, and initial 10 m peak to trough perturbation consisting of a single sinusoid at the dominant wavelength produces an amplification of 12.1. In contrast, an identical simulation with multiple wavelengths in the initial perturbation (including the dominant wavelength) with a maximum peak to trough amplitude of 15 m produces an amplification of 10.2. This decrease in amplification is likely due to complex wavelength interactions as extension occurs. Second, short wavelength topography (~1 km) present in the initial perturbation is not easily removed by unstable extension, and in some cases can still be seen in the final surface deformation. We therefore do not expect unstable extension to completely disrupt features like crater rims. Instead, secondary faulting that accommodates necking (and is not included in this model) must be invoked to explain the complete tectonic resurfacing of vast regions of Enceladus.

The above results suggest that unstable extension can produce moderate amplitude deformation of the surface of Enceladus. Furthermore, instability growth is clearly capable of modifying low amplitude, semi-random terrain into large amplitude periodic ridges and troughs. Such modification may help to explain the existence of many young terrains on Enceladus. However, the greatest amplification produced by our simulations creates ridges and troughs a factor of two or three too low in amplitude to be consistent with our photoclinometric observations of Enceladus' ridges and troughs (Section 2.2). This is especially true for high thermal gradients that produce short-to-moderate wavelength deformation consistent with wavelengths in the Sarandib–Diyar province.

The low amplitude of the deformation produced by unstable extension determined here is consistent with previous results, which indicated that instability growth is a factor of five too low to be consistent with Ganymede's grooved terrain (Bland and Showman, 2007). However, several mechanisms can increase the amplitude of deformation produced by extension. A moderate increase in the amplitude of the initial topography leads to higher amplitude deformation in the extended domain; extension of a surface consisting of random, 30-m average amplitude topography results in ridges and troughs 1.5 times larger than a surface with 10-m initial topography. Furthermore, a surface temperature lower than the 70 K assumed here [perhaps due to a weaker young sun at the time of formation (Showman et al., 1997; Dombard and McKinnon, 2001)] would also increase deformation amplitudes (Bland and Showman, 2007). It is also possible that ice can undergo significant strain or strain-rate softening, which would lead to increased localization of strain within pinched regions and produce greater amplification of the initial topography (Bland and Showman, 2007). Including such processes in simulations of terrestrial extension strongly affects model results (e.g., Buck et al., 2003; Behn et al., 2002; Frederiksen and Braun, 2001; Lavier et al., 2000; Braun et al., 1999; Poliakov and Buck, 1998), in some cases leading to significant increases in localized strain. Thus, while we have not successfully recreated the full amplitude of Enceladus' ridges and troughs, it appears reasonable that unstable extension could have produced the deformation.

5. The heat flux and elastic thickness

The advantage of the unstable extension mechanism remains its ability to produce periodic deformation. The periodicity of the deformation depends strongly on the thermal conditions of the lithosphere. Comparison of photoclinometry and our numerical modeling therefore permits an estimation of the background heat flux present at the time the Sarandib–Diyar province was formed. As described in Section 2.2, dominant wavelengths in both Sarandib Planitia and Diyar Planitia are generally near 3 to 4 km. These wavelengths correspond to a lithospheric thermal gradient of 20 to 40 $K\,km^{-1}$ (Fig. 8), depending on the strain rate assumed. The background heat flux at the time of extension can be estimated from

$$F = k\,\frac{dT}{dz}, \tag{10}$$

where F is the heat flux, dT/dz is the thermal gradient, and $k = (651\ W\,m^{-1})/T$ is the temperature dependent thermal conductivity of ice (Petrenko and Whitworth, 1999, p. 43). Integration of Eq. (10) yields

$$F = \frac{651\ln(T/T_0)}{z}, \tag{11}$$

where T_0 and T are the surface temperature (70 K) and the maximum temperature allowed by our model (180 K), respectively. The depth z is the depth at which the maximum temperature is reached and depends on the imposed thermal gradient: $z = 5.5$ km for $dT/dz = 20\ K\,km^{-1}$, $z = 2.75$ km for $dT/dz = 40\ K\,km^{-1}$. These values suggest heat fluxes of 110 to 220 $mW\,m^{-2}$ in Sarandib and Diyar Planitiea at the time of extension. The Cufa–Láhej region is dominated by longer wavelengths of 4 to 10 km. These wavelengths correspond to thermal gradients of 10 to 20 $K\,km^{-1}$ and heat fluxes of 50 to 110 $mW\,m^{-2}$.

The inferred ancient heat fluxes in Sarandib and Diyar Planitiae are broadly consistent with current heat fluxes measured in the south polar region. Cassini's Composite Infrared Spectrometer (CIRS) measured 3 to 7 GW of thermal emission in the region south of 65° S, corresponding to an average heat flux of 250 $mW\,m^{-2}$ (Spencer et al., 2006). However, caution must be used in making comparisons between the current SPT and the ancient Sarandib–Diyar province. Here we have determined background heat fluxes (averaged over the entire region) while the CIRS observations include significant contributions from highly localized, heterogeneous heat sources: temperature extremes as high as 157 K appear to correlate directly with the tiger stripes (Spencer et al., 2006). Such high temperatures may be the result of shear heating along the tiger stripe fractures (Nimmo et al., 2007). The background heat flux in the SPT may therefore be lower than 250 $mW\,m^{-2}$. Furthermore, it is not clear that necking is applicable to the SPT. While the SPT and the Sarandib–Diyar province share a similar extensional geometry, the fracture-like morphology of the tiger stripes is not predicted by models of unstable extension. The ~30 km spacing between the tiger stripes is much larger than that easily produced by necking at high heat flow, suggesting that neck-

ing is not the dominant factor in determining the spacing of the tiger stripes.

The high heat flux that we infer for the Sarandib–Diyar province at the time of its formation is unlikely to have existed globally. The total power produced by tidal heating of Enceladus in its current orbital state is no more than ∼4 GW, corresponding to a average global surface heat flux of 5 mW m^{-2} (Ross and Schubert, 1989). Thus, evidence of heat fluxes an order of magnitude higher than this value implies a regionally localized heating event, similar to that currently observed at Enceladus' south pole. We find, therefore, that the formation of Sarandib–Diyar province requires a source of both extensional stress and strongly localized heating. These conditions are both met by the existence of a now-inactive diapir within the ice or silicate mantle of Enceladus, as suggested by Helfenstein et al. (2006). Localized heating and melting of the ice mantle, as suggested by Collins and Goodman (2007) is also plausible; however, it is unclear whether the required extensional stress would be generated by this mechanism.

Knowledge of the local thermal gradient and rheological properties of ice allows us to determine elastic thickness (Nimmo et al., 2002) within the Sarandib–Diyar province at the time of their formation. The Maxwell time (τ_M) defines the timescale over which a material will behave elastically. Strains imposed over timescales much smaller than the Maxwell time are accommodated elastically while strains imposed over timescales much longer than the Maxwell time are accommodated viscously. The cross-over point between elastic and viscous behavior occurs when the Deborah number ($D_e = \tau_M \dot{\varepsilon}$, where $\dot{\varepsilon}$ is the strain rate) ∼0.01 (Mancktelow, 1999). Combining the Maxwell time and the non-Newtonian, temperature dependent viscosity of ice [Eq. (7)] yields an expression for the temperature at the base of the elastic layer (i.e. the lithosphere) (Nimmo et al., 2002):

$$T_{\text{base}} = \frac{Q}{nR}\left[\ln\left(\frac{3D_e A^{\frac{1}{n}}\mu}{d^{\frac{m}{n}}\dot{\varepsilon}^{\frac{1}{n}}}\right)\right]^{-1}, \tag{12}$$

where μ is the rigidity modulus ($= E/[2(1+\nu)]$, where E is the Young's modulus and ν is the Poisson ratio), and the other parameters are defined in Section 3. Since the surface temperature (T_s) and thermal gradient ($\mathrm{d}T/\mathrm{d}z$) are known, the elastic thickness, h_e, can be calculated as $h_e = [T_{\text{base}} - T_s]/[\mathrm{d}T/\mathrm{d}z]$.

In the near surface of our simulations, dislocation creep regime C dominates the viscous flow. Using parameters appropriate for this flow law (Table 1), a grain size of 1 mm, a Young's modulus of 10^{10} Pa, and Poisson ratio of 0.25, we calculate temperatures of 86 to 98 K (depending on the strain rate) at the base of the elastic layer. The thermal gradients described above (20 to 40 K km^{-1}) imply elastic thicknesses between 0.4 and 1.4 km. These elastic thicknesses are consistent with the depth to which plastic deformation occurs within the numerical model. A diapir in the ice or silicate mantle has the potential to reorient the satellite if the elastic thickness is greater than 0.5 km (Nimmo and Pappalardo, 2006). Thus, except for the most extreme cases (very high strain rates and thermal gradients), our elastic thickness estimates are great enough to allow reorientation, if such a diapir existed.

6. Conclusions

We have shown that the ridges and troughs of Sarandib–Diyar province likely formed as a result of unstable extension of Enceladus' lithosphere. Unstable extension produces periodically-spaced, undulating pinches and swells. Photoclinometry profiles within the region indicate that, while the deformation in the planitiae is complex, many of the ridges and troughs are, in fact, periodic, with wavelengths between 3 and 4 km in Sarandib and Diyar Planitia, and 4 to 9 km in the Cufa–Láhej region. These simple ridges and troughs are complicated by long wavelength deformation with a variety of morphologies. Shorter wavelengths (1 to 2 km) are also present and are consistent with small-scale fracturing. Average topographic amplitudes in these regions are 100 to 400 m.

Numerical modeling of unstable extension under Enceladus-like conditions indicates that amplifications of the initial topography between factors of 6 and 19 are possible after 31.5% extension. If initial topographic amplitudes were ∼10 m, this implies maximum peak to trough topographic amplitudes of 60 to 190 m after the extension. While these amplitudes are a factor of 2–3 lower than those observed in the topographic profiles, a number of mechanisms can increase amplification rates. We therefore suggest that production of the ridges and troughs of the Sarandib–Diyar province by unstable extension is feasible. Furthermore, we have demonstrated that unstable extension can modify low amplitude (tens of meters) semi-random topography into periodically spaced ridges and troughs, possibly contributing to the tectonic resurfacing of the region.

The modeling results described above are generally comparable to previous modeling results for unstable extension applied to the formation of Ganymede's grooved terrain (Bland and Showman, 2007). However, differences do exist. The maximum amplification produced by unstable extension on Enceladus is 2.5 times greater than the maximum amplification calculated for Ganaymede's grooves. Because of these larger amplifications and Enceladus' lower topographic amplitudes, unstable extension can more easily explain features on Enceladus than on Ganymede. Furthermore, for a given temperature gradient and strain rate, the dominant wavelengths on Enceladus are longer than on Ganymede. These differences are largely due to the difference in gravitational acceleration between the two satellites. Displacing material upward under Enceladus' lower gravity requires less work than under Ganymede's higher gravity. Initial growth rates are therefore higher on Enceladus than on Ganymede, and more total amplification occurs. Additionally, lower hydrostatic stress in Enceladus' lithosphere allow plastic deformation to occur at greater depths than on Ganymede. Because the thickness of the plastic layer controls the wavelength of the deformation, longer dominant wavelengths are produced.

Comparison of dominant wavelengths produced by our numerical models of Enceladus and topographic wavelengths determined from photoclinometry permit estimation of both the heat flux and elastic thickness of the lithosphere at the time resurfacing of the planitiae occurred. We suggest that formation of the ridges and troughs required heat fluxes of 110 to

220 mW m^{-2}. These fluxes require a source of intense tidal heating, which could have triggered extension via diapirism (Nimmo and Pappalardo, 2006), internal phase changes, or other means. Our inferred heat fluxes imply elastic thicknesses of 0.4 to 1.4 km, which are sufficient to allow reorientation of the satellite if the density of the heated region is sufficiently low. This supports the possibility that formation of the Sarandib and Diyar Planitiae, whether by ancient diapirs (Helfenstein et al., 2006) or other mechanisms, caused satellite reorientation. The global reorientation proposed by Nimmo and Pappalardo (2006) might then be but the latest in a series of reorientations that have occurred through Enceladus' history.

Acknowledgments

The authors thank Roger Buck and an anonymous reviewer for thoughtful reviews that strengthened the original manuscript. This research has made use of the USGS Integrated Software for Imagers and Spectometers (ISIS). M.T.B. and A.P.S. were supported by NASA PG&G Grant #NNG04GI46G. R.A.B.'s research was partially supported by an appointment to the NASA Postdoctoral Program at NASA Ames Research Center, administered by Oak Ridge Associated Universities through contract with NASA.

References

Barr, A.C., Pappalardo, R.T., 2005. Onset of convection in the icy Galilean satellites: Influence of rheology. J. Geophys. Res. 110, doi:10.1029/2004JE002371. E12005.

Beeman, M., Durham, W.B., Kirby, S.H., 1988. Friction of ice. J. Geophys. Res. 93, 7625–7633.

Behn, M.D., Lin, J., Zuber, M.T., 2002. A continuum mechanics model for normal faulting using a strain-rate softening rheology: Implications for thermal and rheological controls on continental and oceanic rifting. Earth Planet. Sci. Lett. 202, 725–740.

Beyer, R.A., McEwen, A.S., Kirk, R.L., 2003. Meter-scale slopes of candidate MER landing sites from point photoclinometry. J. Geophys. Res. 108 (E12), doi:10.1029/2003JE002120. 26-1.

Bland, M.T., Showman, A.P., 2007. The formation of Ganymede's grooved terrain: Numerical modeling of extensional necking instabilities. Icarus 189, 439–456.

Braun, J., Chéry, J., Poliakov, A., Mainprice, D., Vauchez, A., Tomassi, A., Daignières, M., 1999. A simple parameterization of strain localization in the ductile regime due to grain size reduction: A case study for olivine. J. Geophys. Res. 104, 25167–25181.

Buck, W.R., Lavier, L.L., Babeyko, A., 2003. A numerical model of lithospheric extension producing fault-bounded basins and ranges. Int. Geol. Rev. 18 (8), 712–713.

Collins, G.C., Goodman, J.C., 2007. Enceladus' south polar sea. Icarus 189, 72–82.

Collins, G.C., Head, J.W., Pappalardo, R.T., 1998. The role of extensional instability in creating Ganymede grooved terrain: Insights from Galileo high-resolution stereo imaging. Geophys. Res. Lett. 25, 233–236.

Dombard, A.J., McKinnon, W.B., 2001. Formation of grooved terrain on Ganymede: Extensional instability mediated by cold, superplastic creep. Icarus 154, 321–336.

Durham, W.B., Kirby, S.H., Stern, L.A., 1997. Creep of water ices at planetary conditions: A compilation. J. Geophys. Res. 102, 16293–16302.

Fink, J.H., Fletcher, R.C., 1981. Variations in thickness of Ganymede's lithoshpere determined by spacings of lineations. Lunar Planet. Sci. XII, 277–278. Abstract.

Fletcher, R.C., Hallet, B., 1983. Unstable extension of the lithosphere: A mechanical model for basin-and-range structure. J. Geophys. Res. 88, 7457–7466.

Frederiksen, S., Braun, J., 2001. Numerical modeling of strain localisation during extension of the continental lithosphere. Earth Planet. Sci. Lett. 188, 241–251.

Gaddis, L., Anderson, J., Becker, K., Becker, T., Cook, D., Edwards, K., Eliason, E., Hare, T., Kieffer, H., Lee, E.M., Mathews, J., Soderblom, L., Sucharski, T., Torson, J., McEwen, A., Robinson, M., 1997. An overview of the Integrated Software for Imaging Spectrometers (ISIS). Lunar Planet. Sci. Conf. XXVIII, 387. Abstract.

Goldsby, D.L., Kohlstedt, D.L., 2001. Superplastic deformation of ice: Experimental observations. J. Geophys. Res. 106, 11017–11030.

Grimm, R.E., Squyres, S.W., 1985. Spectral analysis of groove spacing on Ganymede. J. Geophys. Res. 90. 2013.

Hansen, C.J., Esposito, L., Stewart, A.I.F., Colwell, J., Hendrix, A., Pryor, W., Shemansky, D., West, R., 2006. Enceladus' water vapor plume. Science 311, 1422–1425.

Hapke, B., 1986. Bidirectional reflectance spectroscopy. IV. The extinction coefficient and the opposition effect. Icarus 67, 264–280.

Helfenstein, P., Thomas, P.C., Veverka, J., Porco, C., Giese, B., Wagner, R., Roatsch, T., Denk, T., Neukum, G., Turtle, E., 2006. Surface geology and tectonism on Enceladus. EOS Trans. AGU, Fall Meeting Suppl. 87 (52). Abstract P22B-02.

Herrick, D.L., Stevenson, D.J., 1990. Extensional and compressional instabilities in icy satellite lithospheres. Icarus 85, 191–204.

Janes, D.M., Melosh, H.J., 1988. Sinker tectonics—An approach to the surface of Miranda. J. Geophys. Res. 93, 3127–3143.

Kargel, J.S., Pozio, S., 1996. The volcanic and tectonic history of Enceladus. Icarus 119, 385–404.

Kirby, S.H., Durham, W.B., Beeman, M.L., Heard, H.C., Daley, M.A., 1987. Inelastic properties of ice I_h at low temperatures and high pressures. J. Phys. 48, 227–232.

Lavier, L.L., Buck, W.R., Poliakov, A.N.B., 2000. Factors controlling normal fault offset in an ideal brittle layer. J. Geophys. Res. 105, 23431–23442.

Lissauer, J.J., Peale, S.J., Cuzzi, J.N., 1984. Ring torque on Janus and the melting of Enceladus. Icarus 58, 159–168.

Mancktelow, N.S., 1999. Finite-element modelling of single-layer folding in elasto-viscous materials: The effect of initial perturbation geometry. J. Struct. Geol. 21, 161–177.

McEwen, A.S., 1991. Photometric functions for photoclinometry and other applications. Icarus 92, 298–311.

Melosh, H.J., Raefsky, A., 1980. The dynamical origin of subduction zone topography. Geophys. J. R. Astron. Soc. 60, 333–354.

Meyer, J., Wisdom, J., 2007. Tidal heating in Enceladus. Icarus 188, 535–539.

Nimmo, F., Pappalardo, R.T., 2006. Diapir-induced reorientation of Saturn's moon Enceladus. Nature 441, 614–616.

Nimmo, F., Pappalardo, R.T., Giese, B., 2002. Effective elastic thickness and heat flux estimates on Ganymede. Geophys. Res. Lett. 29, doi:10.1029/2001GL013976, 1158.

Nimmo, F., Spencer, J.R., Pappalardo, R.T., Mullen, M.E., 2007. Shear heating as the origin of the plumes and heat flux on Enceladus. Nature 447, 289–291.

Pappalardo, R.T., Greeley, R., 1995. A review of the origins of subparallel ridges and troughs: Generalized morphological predictions from terrestrial models. J. Geophys. Res. 100, 18985–19007.

Pappalardo, R.T., Head, J.W., Collins, G.C., Kirk, R.L., Neukum, G., Oberst, J., Giese, B., Greeley, R., Chapman, C.R., Helfenstein, P., Moore, J.M., McEwen, A., Tufts, B.R., Senske, D.A., Breneman, H.H., Klaasen, K., 1998. Grooved terrain on Ganymede: First results from Galileo high-resolution imaging. Icarus 135, 276–302.

Passey, Q.R., 1983. Viscosity of the lithosphere of Enceladus. Icarus 53, 105–120.

Patel, J.G., Pappalardo, R.T., Head, J.W., Collins, G.C., Hiesinger, H., Sun, J., 1999. Topographic wavelengths of Ganymede groove lanes from Fourier analysis of Galileo images. J. Geophys. Res. 104, 24057–24074.

Petrenko, V.F., Whitworth, R.W., 1999. Physics of Ice. Oxford Univ. Press, Oxford.

Plescia, J.B., Boyce, J.M., 1983. Crater numbers and geological histories of Iapetus, Enceladus, Tethys and Hyperion. Nature 301, 666–670.

Poliakov, A.N.B., Buck, W.R., 1998. Mechanics of stretching elastic–plastic–viscous layers: Applications to slow-spreading mid-ocean ridges. In: Buck, W.R., Delaney, P.T., Karson, J.A., Lagabrielle, Y. (Eds.), Faulting and Magmatism at Mid-Ocean Ridges. American Geophysical Union, Washington, DC, pp. 305–323.

Porco, C.C., West, R.A., Squyres, S., McEwen, A., Thomas, P., Murray, C.D., Delgenio, A., Ingersoll, A.P., Johnson, T.V., Neukum, G., Veverka, J., Dones, L., Brahic, A., Burns, J.A., Haemmerle, V., Knowles, B., Dawson, D., Roatsch, T., Beurle, K., Owen, W., 2004. Cassini imaging science: Instrument characteristics and anticipated scientific investigations at Saturn. Space Sci. Rev. 115, 363–497.

Porco, C., Adams, S.L., Diehl, J.M., Knowles, B.D., Pieri, L.J., Riley, J.J., 2005a. Cassini Orbiter Calibration ISSNA/ISSWA 2 EDR, Version 1.0. CO-CAL-ISSNA/ISSWA-2-EDR-V1.0, COISS_0011. NASA Planetary Data System.

Porco, C., Adams, S.L., Diehl, J.M., Knowles, B.D., Pieri, L.J., Riley, J.J., 2005b. Cassini Orbiter Saturn ISSNA/ISSWA 2 EDR, Version 1.0. CO-S-ISSNA/ISSWA-2-EDR-V1.0. NASA Planetary Data System.

Porco, C.C., Helfenstein, P., Thomas, P.C., Ingersoll, A.P., Wisdom, J., West, R., Neukum, G., Denk, T., Wagner, R., Roatsch, T., Kieffer, S., Turtle, E., McEwen, A., Johnson, T.V., Rathbun, J., Veverka, J., Wilson, D., Perry, J., Spitale, J., Brahic, A., Burns, J.A., DelGenio, A.D., Dones, L., Murray, C.D., Squyres, S., 2006. Cassini observes the active south pole of Enceladus. Science 311, 1393–1401.

Ranalli, G., 1995. Rheology of the Earth. Chapman and Hall, London.

Ross, M.N., Schubert, G., 1989. Viscoelastic models of tidal heating in Enceladus. Icarus 78, 90–101.

Showman, A.P., Stevenson, D.J., Malhotra, R., 1997. Coupled orbital and thermal evolution of Ganymede. Icarus 129, 367–383.

Spencer, J.R., Pearl, J.C., Segura, M., Flasar, F.M., Mamoutkine, A., Romani, P., Buratti, B.J., Hendrix, A.R., Spilker, L.J., Lopes, R.M.C., 2006. Cassini encounters Enceladus: Background and the discovery of a south polar hot spot. Science 311, 1401–1405.

Squyres, S.W., 1981. The topography of Ganymede's grooved terrain. Icarus 46, 156–168.

Squyres, S.W., Reynolds, R.T., Cassen, P.M., Peale, S.J., 1983. The evolution of Enceladus. Icarus 53, 319–331.

USGS, 2007. Integrated Software for Imagers and Spectrometers (ISIS). US Geological Survey, Flagstaff, AZ, http://isis.astrogeology.usgs.gov/.

Verbiscer, A.J., Veverka, J., 1994. A photometric study of Enceladus. Icarus 110, 155–164.

Wisdom, J., 2004. Spin–orbit secondary resonance dynamics of Enceladus. Astron. J. 128, 484–491.

Yoder, C.F., 1979. How tidal heating on Io drives the Galilean orbital resonance locks. Nature 279, 767–770.